# Red Nuggets at $z \sim 1.5$ : Compact passive galaxies and the formation of the Kormendy Relation

Ivana Damjanov<sup>†</sup>, Patrick J. McCarthy<sup>‡</sup>, Roberto G. Abraham<sup>†</sup>, Karl Glazebrook<sup>¶</sup>, Haojing Yan<sup>‡</sup>, Erin Mentuch<sup>†</sup>, Damien Le Borgne<sup>⋄</sup>, Sandra Savaglio<sup>§</sup>, David Crampton<sup>⋄</sup>, Richard Murowinski<sup>⋄</sup>, Stéphanie Juneau<sup>⊙</sup>, R. G. Carlberg<sup>†</sup>, Inger Jørgensen<sup>⋄</sup>, Kathy Roth<sup>⋄</sup>, Hsiao-Wen Chen<sup>⋄</sup>, and Ronald O. Marzke<sup>⋆</sup>

### **ABSTRACT**

We present the results of NICMOS imaging of a sample of 19 high mass passively evolving galaxies with 1.2 < z < 2, taken primarily from the Gemini Deep Deep Survey (GDDS). Around 80% of galaxies in our GDDS sample have spectra dominated by stars with ages  $\gtrsim 1$  Gyr. Our rest-frame R-band images show that most of these objects have compact regular morphologies which follow the classical  $R^{1/4}$  law. These galaxies scatter along a tight sequence in the size vs. surface brightness parameter space which defines the Kormendy relation. Around one-third (3/10) of the massive red objects in the GDDS sample are extraordinarily compact, with effective radii under one kiloparsec. Our NICMOS observations allow the detection of such systems more robustly than is possible with optical (rest-frame UV) data, and while similar systems have been seen at  $z \geq 2$ , this is the first time such systems have been detected in a rest-frame optical survey at 1.2 < z < 2. We refer to these compact galaxies as 'red nuggets', and note that similarly compact massive galaxies are completely absent in the nearby Universe. We introduce a new 'stellar mass Kormendy relation' (stellar mass density vs size) which we use to single out the effects of size evolution from those of luminosity and color evolution in stellar populations. The 1 < z < 2 passive galaxies have mass densities that are an order of magnitude larger then early type galaxies today and are comparable to the compact distant red galaxies at 2 < z < 3. We briefly consider mechanisms for size evolution in contemporary models focusing on equalmass mergers and adiabatic expansion driven by stellar mass loss. Neither of these mechanisms appears able to transform the high-redshift Kormendy relation into its local counterpart, leaving the origin and fate of these compact 'red nuggets' unresolved.

Subject headings: galaxies: elliptical, galaxies: fundamental parameters, galaxies: evolution

<sup>&</sup>lt;sup>†</sup>Department of Astronomy & Astrophysics, University of Toronto, 50 St. George Street, Toronto, ON, M5S 3H4

<sup>&</sup>lt;sup>‡</sup>Observatories of the Carnegie Institution of Washington,813 Santa Barbara Street, Pasadena, CA 91101

<sup>¶</sup>Centre for Astrophysics and Supercomputing, Swinburne University of Technology, 1 Alfred St, Hawthorn, Victoria 3122, Australia

<sup>§</sup>Max-Planck-Institut für extraterrestrische Physik, Garching, Germany

<sup>°</sup>Herzberg Institute of Astrophysics, National Research Council, 5071 West Saanich Road, Victoria, British Columbia, V9E 2E7, Canada.

 $<sup>{}^{\</sup>odot}\textsc{Department}$  of Astronomy /Steward Observatory, Uni-

versity of Arizona, 933 N Cherry Ave., Rm. N204, Tucson AZ 85721-0065

<sup>°</sup>DSM/ DAPNIA/ Service d'Astrophysique, CEA/ SACLAY, 91191 Gif-sur-Yvette Cedex, France

<sup>&</sup>lt;sup>▷</sup>Gemini Observatory, Hilo, HI 96720

<sup>^</sup>The Department of Astonomy and Astrophysics, University of Chicago, 5640 S. Ellis Ave, Chicago, IL 60637

<sup>\*</sup>Dept. of Physics and Astronomy, San Francisco State University, 1600 Holloway Avenue, San Francisco, CA 94132

#### 1. Introduction

The formation mechanism of elliptical galaxies has long been controversial and remains a key test of more general galaxy formation models. The original 'nature' (Eggen, Lynden-Bell & Sandage (1962) monolithic collapse) vs. 'nurture' (formation through mergers, (e.g., Schweizer 1987; Searle & Zinn 1978; Toomre & Toomre 1972) debate is still with us, but is now set in a ΛCDM cosmological context which attempts to connect the stellar component of galaxies to an underlying evolutionary picture for the clustering of dark matter halos. Testing this model requires studying the evolution of galaxies over a large redshift range.

A wide range of selection techniques have been effective in selecting galaxies in various redshift ranges on the basis of their current star formation rates (e.g. Lyman break galaxies, submm sources etc), or from the spectral signatures of passively evolving old stellar populations (e.g., extremely red objects (EROs) and other color selections). The most massive local elliptical galaxies have the oldest stellar populations (Gallagher, Hunter & Tutukov 1984), so identifying the progenitors of local early-type galaxies within the high-redshift galaxy population is of particular interest. There is a consensus that the mass density in the red sequence is evolving strongly in the 1 < z < 2 range (GDDS Paper VIII, Abraham et al. 2007; GDDS Paper III, Glazebrook et al. 2004; Fontana et al. 2004; Rudnick et al. 2003), a process that continues at redshifts below unity as well (Faber et al. 2007; Bell et al. 2004), although the magnitude of the evolution is uncertain (Brown et al. 2007; Chen et al. 2003). Massive morphologicallyconfirmed elliptical galaxies have been found up to z = 2 (GDDS Paper IV, McCarthy et al. 2004; Cimatti et al. 2004) with spectra consistent with formation epochs up to z > 5. These observations were in in direct contradiction with early  $\Lambda$ CDM models where stellar mass assembly traced the build up of cold dark matter haloes, although additional feedback mechanisms on the baryons have more recently been able to better account for this (e.g., Kang, Jing, & Silk 2006). A complication recently added to this picture is the observation that the space density of ellipticals is found

to evolve strongly over 1 < z < 2 (Paper VIII) even while their stellar populations evolve weakly, suggesting that one must be careful to decouple morphological evolution from evolution of the underlying stellar populations. This is seen at higher redshifts also, where the paucity of passively evolving galaxies at z > 2 in deep J - Kand 3.5  $\mu$ m selected samples (Kriek et al. 2006; Labbé et al. 2005; Cimatti et al. 2002) shows that the assembly epoch for the red sequence may be decoupled from the epoch of the earliest star formation. Studies of star formation history and morphology can only go so far in unraveling the puzzle of galaxy formation; dynamical and chemical probes are needed to connect progenitors to descendants. Clustering signatures offer one dynamical approach to connecting progenitors to descendants and the strong clustering of the passive red galaxies (Daddi et al. 2005a, 2004; Brown et al. 2003; McCarthy et al. 2001) strongly suggest that they are linked to today's massive ellipitical galaxies.

Theoretical attempts to explain these observations have resulted in greatly improved  $\Lambda$ CDM models which decouple mass assembly from this stellar population downsizing. An example is the semi-analytic model of De Lucia & Blaizot Here the small ellipticals and their stars form early by disc mergers. Massive ellipticals can then grow bigger and more numerous at late times through dissipationless or dry This may even have been observed merging. (Bell et al. 2006a) though there is some disagreement as to whether the  $\Lambda$ CDM merger rate is high enough (Bundy et al. 2007). At this stage it is perhaps fair to say that dry merging simulations show that it does not disrupt elliptical scaling relations (Boylan-Kolchin et al. 2006, 2005; González-García & van Albada 2003) as one might naively expect. However only a limited number of simulations of this process have been done and they have not yet been incorporated into cosmological models in a detailed way such that they can be compared with data (e.g., numbers, sizes and masses of galaxies). Further it is not clear that a dry merging hierarchy consistent with cosmological downsizing can also be made consistent with the evolving mass-metallicity relation (Pipino and Matteucci 2008). A contrasting picture is painted by Naab et al. (2007) using a SPH model of individual systems. They argue for a formation mode dominated by something very close to early monolithic collapse, but in a  $\Lambda$ CDM cosmological context, with mergers (along with accretion) playing only a minor role in stellar mass growth at late times.

High spatial resolution studies of the morphologies and structures of passive galaxies offer one approach to gauging the importance of recent major merger events. A number of studies with the Hubble Space Telescope (HST) have shown that half or more of red galaxies in color-selected samples have simple early type morphologies. Most of these studies are confined to redshifts of  $\sim 1.5$  and less, and the early-type fraction varies from  $\sim 50\%$ to 70% (Moustakas et al. 2004; Yan & Thompson At higher redshifts a significant fraction of the red galaxies appear to be discs (e.g., Paper VIII, Fontana et al. 2004). Understanding the connection between these two classes of objects naturally focuses on the importance of mergers, since nearly equal-mass mergers are thought to transform discs into spheroids. Mergers, both gas-rich and dissipationless, are also thought to be important in the growth of the red sequence and evidence, both direct and indirect, supports that this is occurring at intermediate and low redshifts (e.g., Bell et al. 2006b, and the references therein). It appears that much of the high-redshift merging activity may be of the dissipationless variety where the main effect of merging is to reorganize existing stellar population without triggering new star formation. It is difficult to envision how this might operate unless the merging systems are themselves gas-poor, which is not generally expected (van Dokkum 2005). In any case, the signatures of such 'dry' mergers are difficult to detect at high redshifts.

Recently, several imaging studies have shown that red galaxies at z>1 appear smaller than their likely present-day descendants with the same stellar mass (Longhetti et al. 2007; Cimatti et al. 2008). The implications of these observations are seen most clearly in the structural and dynamical scaling relations, the Fundamental Plane and its projections (the Faber-Jackson (1976) and Kormendy (1977) relations). In the present paper we explore the nature of the Kormendy relation, (mean surface brightness within the effective radius,  $\langle \mu \rangle_e$ , versus effective radius,  $R_e$ ). This

is the most observationally accessible projection of the fundamental plane at high-redshift. Our analysis spans the redshift range 1.2 < z < 2using HST NICMOS observations of a sample of quiescent high-redshift galaxies taken mainly from the Gemini Deep Deep Survey (GDDS Paper I, Abraham et al. 2004). We present NICMOS F160W images for ten of the twenty z > 1.3 passive red galaxies from Paper IV. These systems all have spectra dominated by old stellar populations. This extends to higher redshifts (z > 1.7)than the earlier NICMOS work of Longhetti et al. (2007) from the Munich Near-IR Cluster Survey (MUNICS, Drory et al. 2001). We also independently analyze the archival NICMOS data of Longhetti et al. (2007) in the redshift range 1.2 < z < 1.7 to supplement our sample and confirm their findings. At the higher redshifts previous findings of compact galaxies were based on optical data obtained with the Advanced Camera for Surveys (ACS) onboard HST (Cimatti et al. 2008). Our use of NICMOS allows us to more robustly show that the old components in the galaxies are truly compact. Finally, we are able to unify the optical and infrared work by introducing a new 'stellar mass Kormendy relation' which we use to better quantify evolution in the sizes of early-type galaxies as a function of stellar mass over the redshift range 1 < z < 2. We briefly examine the likelihood that dry mergers explain such size evolution, and examine whether an alternative process, adiabatic expansion, might be more important. We describe the observations in section 2, our analysis in section 3, and present our results in section 4. In section 5 we discuss the implications of our observations for simple models for galaxy size growth. Throughout we use standard cosmological parameters;  $H_0 = 70 \text{ km s}^{-1} \text{ Mpc}^{-1}$ ,  $\Omega_{\rm m} = 0.3, \, \Omega_{\Lambda} = 0.7.$  Unless stated otherwise, all magnitudes are based on the AB system.

### 2. Description of the Observations

#### 2.1. Sample definition

Our sample of galaxies was taken mainly from the GDDS, crafted to sample the galaxy population in the critical 1 < z < 2 interval with an emphasis on red galaxies (Paper I). While modest in area (120 square arcminutes), the survey is spread over four independent and representative

sightlines. Redshifts for  $\sim 300$  galaxies brighter than I(Vega) = 24.5 were obtained from 30-hour long integrations using the GMOS spectrometer on Gemini North. This magnitude limit corresponds to the stellar mass of  $2.5 \times 10^{10} \ \mathrm{M}_{\odot}$  for a galaxy with the redshift of formation  $z_f = 10$ and maximally old stellar population observed at redshift z = 1.5 (Paper III). We classified the galaxies on the basis of their spectra, depending on whether they were dominated by active star formation, stars older than  $\sim 1$  Gyr, intermediate age (0.3-1 Gyr) populations, or a mix of these types. Of the 302 galaxies with redshifts, 47 have spectra dominated by old stars, and twenty of these lie at redshifts beyond 1.3. Spectra of these twenty galaxies and estimates of their ages and formation redshifts are presented in Paper IV. Deep I-band images of the GDDS galaxies at z < 1.7 with the ACS on HST reveal that the correlation between spectral type, and hence stellar content, and morphological class seen at present is strong at these redshifts. Nearly all of the GDDS galaxies with passive spectral classes have compact morphologies consistent with early Hubble types, while the actively star forming galaxies have a morphologies that range from simple disks to complex structures indicative of ongoing mergers. The GDDS galaxies discussed in this paper are a subset of the GDDS galaxies having spectra dominated by old stars (class "001" from Paper I) and z > 1.3. The key properties of this sample are given in Table 1.

Our primary sample of ten galaxies is drawn from the GDDS and determined by the number of available orbits and the desired depth of NIC-MOS imaging. The targets were selected randomly, with the exception of the two (12-5869) and 12-5592) that could be covered in a single pointing. We also analyzed archival data from the MUNICS survey for nine additional galaxies with properties similar to those of our GDDS sample. Longhetti et al. (2005) analyzed spectrophotometric data set for these galaxies from the nearinfared spectroscopic follow-up of a complete sample of bright (K < 18.5) EROs (R - K > 5.3)selected from the MUNICS survey<sup>1</sup>. Low resolution spectroscopic and photometric data revealed stellar masses greater than  $10^{11} M_{\odot}$  and dominant

old stellar population for all objects in the sample (see Table 2). As will be described below, this additional data provided us with a useful check of our methodology by allowing us to compare results from our analysis pipeline against those published in Longhetti et al. (2007).

#### 2.2. NICMOS Observations

The ten GDDS galaxies were observed with Camera 3 on NICMOS using the F160W filter. Each individual exposure was 896 seconds in duration with multiple samples using the STEP64 read pattern. A single orbit contained three exposures and we observed each target over four HST orbits for a total integration time of 10740 seconds. Two of the fields overlapped and the images for targets 12-5869 and 12-5592 have twice the exposure time of the others. These objects are discussed in detail in McCarthy et al. (2007). We dithered in non-integer pixel steps between each exposure. The individual frames were dark corrected, sky subtracted and combined using the DRIZZLE algorithm (Fruchter & Hook 2002) with a final pixel size of 0.12. Residual sky levels in the final mosaics were derived from Gaussian fits to a histogram of sky values and were subtracted.

As noted above, we also re-analyised nine galaxies from the MUNICS sample of red galaxies described in Longhetti et al. (2007). The MUNICS data set was obtained using Camera 2 on NIC-MOS, and is thus more finely sampled, and somewhat shallower, than our NIC3 images. As described below, analyzing this NIC2 data allowed us to explore, and ultimately rule out, the possibility that the coarser sampling of our NIC3 data might lead to poor model fits and spurious sizes. We retrieved the pipeline-processed individual NIC2 images from the HST archive. We then corrected each image for residual pedestal effects and combined them into mosaics using the DRIZZLE algorithm with a final pixel size of 0.05. The properties of the nine galaxies in this sample are summarized in Table 2.

#### 3. Analysis

#### 3.1. Surface brightness profiles

Using the Galfit software package (Peng et al. 2002), we derived two-dimensional (2D) surface

 $<sup>^1{\</sup>rm This}$  is actually a blank field survey, the intention was to  $find~{\rm high}\textsc{-}z$  clusters from deep wide-field near-IR imaging.

 $\begin{tabular}{ll} Table 1 \\ Properties of the ten galaxies in GDDS sample \\ \end{tabular}$ 

ID	z	${\rm Mass^a} \\ [10^{11} \ {\rm M}_{\odot}]$	$Age^b$ $[Gyr]$
12-5592 12-5869 12-6072 12-8025 12-8895 15-4367 15-5005 15-7543 22-0189 22-1983	1.623 1.51 1.576 1.397 1.646 1.725 1.845 1.801 1.49	$1.16 \pm 0.27$ $3.14 \pm 0.43$ $0.59 \pm 0.27$ $1.25 \pm 0.39$ $3.18 \pm 0.44$ $0.56 \pm 0.15$ $0.67 \pm 0.24$ $1.06 \pm 0.30$ $2.85 \pm 0.98$ $1.34 \pm 0.53$	$\begin{array}{c} 1.1^{+0.3}_{-0.4} \\ 1.2^{+0.6}_{-0.2} \\ 1.6^{+2.1}_{-1.3} \\ 0.8^{+0.6}_{-0.1} \\ 2.5^{+0.3}_{-0.3} \\ 2.1^{+0.4}_{-0.9} \\ 0.5^{+0.7}_{-0.1} \\ 0.9^{+0.5}_{-0.2} \\ 3.0^{+0.7}_{-0.2} \\ 1.1^{+3.1}_{-0.5} \end{array}$

 $<sup>^{\</sup>rm a}$  GDDS mass estimates are based on the Baldry & Glazebrook (2003) IMF, and taken from Paper III

 $\label{eq:Table 2} Table \ 2$  Properties of Six massive galaxies in MUNICS sample  $^{\rm a}$ 

ID	z	${\rm Mass^b} \\ [10^{11} \ {\rm M}_{\odot}]$	Age [Gyr]
S2F5_109 S7F5_254 S2F1_357 S2F1_389 S2F1_511 S2F1_142 S7F5_045 S2F1_633 S2F1_443	1.22 1.34 1.40 1.40 1.43 1.45 1.45	$5.94 \pm 0.95$ $4.68 \pm 0.16$ $4.65 \pm 0.40$ $2.15 \pm 0.86$ $2.07 \pm 0.89$ $4.06 \pm 0.94$ $3.58 \pm 1.10$ $3.52 \pm 0.51$ $3.58 \pm 1.48$	$1.7 \pm 0.3$ $5.0 \pm 0.1$ $4.0 \pm 0.1$ $3.0 \pm 0.5$ $1.3 \pm 0.3$ $2.2 \pm 0.2$ $1.7 \pm 0.3$ $4.0 \pm 0.5$ $3.5 \pm 0.3$

<sup>&</sup>lt;sup>a</sup> from Longhetti et al. (2007)

 $<sup>^{\</sup>rm b}$  Minimum galaxy ages from Paper IV

<sup>&</sup>lt;sup>b</sup> MUNICS mass estimates are taken from Longhetti et al. (2005, Salpeter IMF), and transformed to Baldry & Glazebrook (2003) IMF following the relation given in Paper III

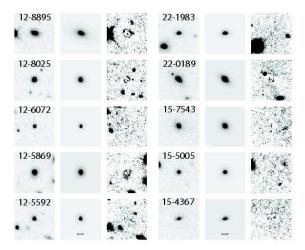


Fig. 1.—NIC3 images and the results of our 2D fitting with Galfit for our sample of 10 GDDS galaxies with 1.3 < z < 2 and spectra dominated by old stars. The three columns present the drizzled F160W image, the best fitting  $\mathbb{R}^{1/4}$  model, and the residuals. The residual images have been scaled by a factor of 10 compared to the data and models to bring out faint features. The bars at the bottom are one arcsecond in length.

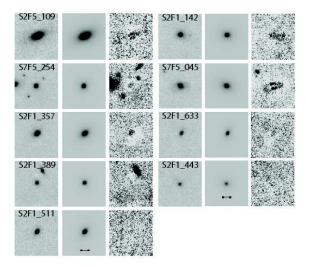


Fig. 2.— NIC2 images and the results of our 2D fitting with Galfit of the six galaxies from Longhetti et al. (2007). The three columns present the galaxy, the best fitting  $R^{1/4}$  model, and the residuals. The residual images have been scaled by a factor of 10 compared to the data and models to bring out faint features. The bars at the bottom are one arcsecond in length.

brightness profiles by fitting synthetic galaxy images to our data using a range of surface brightness profiles, ellipticities and orientations. A series of models were constructed using exponential surface brightness profiles, de Vaucouleurs  $R^{1/4}$ profiles and the more general  $\mathbb{R}^{1/n}$  Sérsic profiles. We did not consider more general fitting laws due to the relatively small range of radii (0''.12 - 2''), or 1 - 17 kpc at z = 1.5) covered by our observations. Models with a range of scale lengths and eccentricities were convolved with the Point Spread Function (PSF) of the observations and subtracted from the NICMOS images. We used PSFs derived from well-detected unsaturated stars in each NIC3 field rather than the TinyTim simulations as we found the former produced better fits. The residuals were computed and the model parameters were iterated to minimize the square of the residuals within the box of  $8''.4 \times 8''.4$  centered on each galaxy. The initial guess for the centroid was the position of the highest intensity pixel within the fitting box, and the total magnitude was estimated according to the total intensity confined in this box. Both initial guesses were made after masking out of the neighbouring sources. The root mean square (RMS) image was used to give relative weights to the background pixels during the fitting. By using different stars the width of the NIC3 PSF was allowed to vary to include the effects of spatial and temporal variations in the NIC3 PSF. Changing the PSF had very little impact on the derived effective radii in all cases. The best-fit models for all galaxies in the sample are presented in Figure 1 (middle column) along with the residual images (last column). Parameters of the best-fit  $R^{1/4}$  and  $R^{1/n}$  profiles for each galaxy are given in Table 3. The listed minima of reduced  $\chi^2$  are well below unity, suggesting that the flux uncertainties introduced by the RMS images are overestimated. We performed the same morphological analysis on the MUNICS galaxies (Longhetti et al. 2007). The NIC2 PSF used for modeling 2D profiles of these objects was derived from the TinyTim simulations. The resulting best-fit  $R^{1/4}$  profiles are graphically illustrated in Figure 2. The parameters obtained are listed in Table 4, along with the results from Longhetti et al. (2007) for comparison. The reduced  $\chi^2$  are again below unity, but the values obtained for our best fit are very similar to the

ones obtained for Longhetti et al. (2007) parameters, except for the total F160W magnitudes where the difference is greater than  $1\sigma$ . The reasons for this discrepancy may be the simulated PSF we used for 2D fitting and the different methods applied for background subtraction. Also, resulting  $R^{1/4}$  fit effective radius  $R_e$  and surface brightness  $\langle \mu \rangle_e$  for objects S2F1\_142, S7F5\_45, S2F1\_633, and S2F1\_443 differ for more then  $1\sigma$  from the previously reported ones. When fitted with  $R^{1/n}$  profiles, the best fits for the three of these objects -S2F1\_142, S2F1\_633, and S7F5\_45 - have lower indices n than listed in Longhetti et al. (2007) - 2 instead of 3.5, 2.5 instead of 4.1, and 1.5 instead of 2, respectively. On the other hand, the best fit  $R^{1/n}$  profile for S2F1\_443 has index n = 2.8, higher than n = 1.9 reported by Longhetti et al. (2007). For the rest of the MUNICS sample the difference in the goodness of fit for  $\mathbb{R}^{1/4}$  profile between our and Longhetti et al. (2007) analysis is  $\Delta(\chi^2) \lesssim 0.2.$ 

As a consistancy check, we also determined onedimensional (1D) azimuthally averaged radial surface brightness profiles for each galaxy and for the corresponding models resulting from its 2D profile fits. These 1D radial profiles were extracted using the approach developed by Jedrzejewski (1987) as implemented in IRAF (Tody 1993). Integrated magnitudes were determined within a series of elliptical isophotes, the spacing of which grows with radius. We masked objects closer than 10" before determining the surface brightness profiles of the galaxies. In most cases we are able to determine the profile over roughly six magnitudes of surface brightness and to radii of 1"5, or  $\sim 13$  kpc at z = 1.5. The  $5\sigma$  limiting surface brightness for most of our observations is  $\mu_{F160} \approx 23$ mag  $\operatorname{arcsec}^{-2}$ ; the data for 12-5869 and 12-5592 reach approximately 0.3 magnitudes deeper. This surface brightness limit corresponds to  $\mu_r \approx 20$ mag arcsec<sup>-2</sup> ( $\mu_r \approx 20.3$  mag arcsec<sup>-2</sup> for 12-5869 and 12-5592) for a galaxy at redshift z = 1.5that is formed at  $z_f = 6$  with exponentially declining SFR and e-folding time  $\tau = 0.1$  Gyr. Surface brightness profiles were determined in a similar fashion for each star that served as a local measure of the PSF. Azimuthally averaged surface brightness profiles for all of our GDDS objects are presented in Figure 3, with the profiles of best-fitting 2D models and a PSF profile shown as solid lines

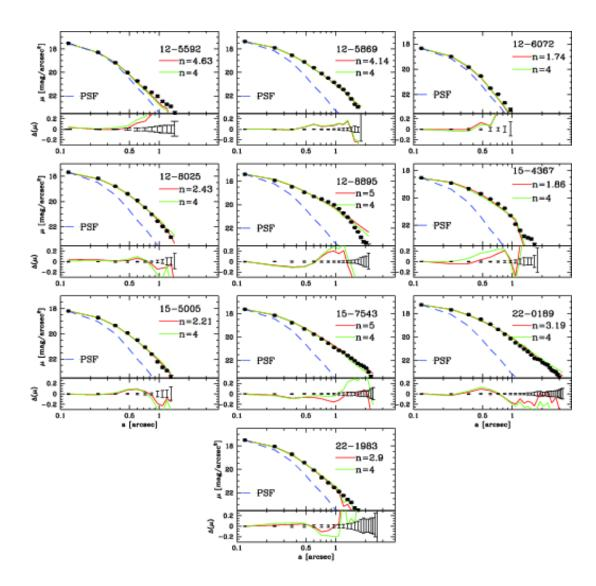


Fig. 3.— Upper panels: major axis surface brightness profiles in the F160W band for each galaxy (squares), with  $R^{1/4}$  (green line) best-fit profile,  $R^{1/n}$  (red line) best-fit profile, and a PSF profile (blue dashed line) overploted. The step used to present isophotal surface brightness corresponds to the pixel scale of our drizzled NIC3 images (0″.12). The limiting surface brightness in each panel presents (roughly)  $5\sigma$  limit for our observations. The lower part of each panel shows the residual differences between the data points and the model fits, with the 1  $\sigma$  errors on the data shown for comparison.

and a dashed line, respectively. Figure 3 confirms that all galaxies in our GDDS sample are well resolved, except for the target 12-6072 that seems only marginally resolved when compared to the PSF 1D profile. The profiles are smooth in nearly all cases, the exception being object 15-4367 which shows a step at a = 1".5. Careful examination of this obejct's NIC3 image revealed that it was not perfectly symmetric and harboured a weak disk. The best  $\mathbf{R}^{1/n}$  profile index of  $\sim 2$  confirms these findings. In addition, 15-4367 has a very faint neighbouring object that had to be masked out before fitting. These two effects produced the step in its 1D profile seen in Fig. 3.

In order to estimate the errors on parameters obtained by our 2D and 1D fitting procedures, we undertook a series of Monte Carlo (MC) simulations which incorporated all the sources of systematic and random errors we were able to identify. We constructed a set of galaxy images from our best-fit model for each galaxy and convolved these with a range of PSFs (i.e., PSFs obtained from different stars) and added these to the background images. We dithered the position image about the central value to explore the importance of binning, and used RMS images to construct 2D arrays of random numbers to capture poisson noise and structure in the sky background. Each image constructed in this way went through the same fitting procedure as the real galaxy image from our sample. The standard deviations of resulting parameters are shown as the error estimates reported in Table 3. The reduced  $\chi^2$  values for the best fits to the MC simulations are of the order of unity and larger then reduced  $\chi^2$  of the best fits to the data, which makes our error estimates very conservative.

# 3.2. K-corrections and cosmological dimming

Our analysis requires comparison between the properties of our 1.2 < z < 2 samples observed at  $1.6~\mu m$  (H-band) to those of present-day galaxies observed at visible wavelengths. In order to make a proper comparison, we need to transform the various data sets to a common bandpass and apply a K-correction. We computed appropriate spectral energy distributions (SEDs) using PEGASE-HR spectral synthesis models (Le Borgne et al. 2004). The model that we used is based on the

Baldry & Glazebrook (2003) initial mass function (IMF), solar metallicity, and an exponentially declining star formation rate with a time scale of  $\tau = 0.1$  Gyr, very similar to a single burst. The typical ages of GDDS and MUNICS passive galaxies at 1.2 < z < 2 are 3 - 4 Gyr (Paper IV, Longhetti et al. 2005) and we used a 4 Gyr model to approximate their SED. It is important to emphasize that the correction needed to reduce our H-band data to rest-frame SDSS-r is remarkably insensitive to SED shape since redshifted H-band closely matches rest-frame SDSS-r at  $z\sim 1.5$ . The photometry for the two samples is listed in Tables 3 and 4. Cosmological surface brightness dimming will reduce the observed surface brightness and these must be corrected by  $(1+z)^4$  to transform them to the rest-frame.

#### 4. Results

### 4.1. Morphologies of Passive Galaxies at z > 1.3

All of the objects in our NICMOS F160W sample (shown in Figures 1 and 2) have compact morphologies and none show obvious evidence of interactions, such as double nuclei or disturbed isophotes at bright levels. The star-forming massive galaxies drawn from the GDDS sample, by contrast, exhibit a wide range of disturbed morphologies as shown in Paper VIII. The intermediate age and composite population systems primarily have disk morphologies, while the passive galaxies at z < 1.3 discussed in Paper VIII exhibit a preponderance for compact and regular morphologies. Six of the 10 GDDS galaxies in the present sample appear to be early types with  $R^{1/n}$ profile index n > 2.5 (Table 3), while the four potential disk systems in our z > 1.3 passive sample appear to have prominent bulges. Thus 60% of our GDDS sample defined by spectral properties have pure early type morphologies, and this fraction rises to 90% when the prominent bulges with very weak disks are also taken into account as early type object. To a first approximation, our NICMOS Camera 3 images extend the correlation between spectra indicative of old stellar populations and compact early-type morphologies from  $z \sim 1.3$  to  $z \sim 2$ . This is not surprising given previous indications in this direction from smaller samples (e.g., Cimatti et al. 2004).

 ${\it TABLE~3}$  Morphological parameters of the galaxies in the GDDS sample

ID	F160W [mag]	n	$r_e$ [arcsec]	$R_e$ [kpc]	$\langle \mu \rangle_e^{160W}$ [mag/arcsec <sup>2</sup> ]	$\langle \mu \rangle_e^{corr}$ [mag/arcsec <sup>2</sup> ]	b/a	$\chi^2$
12-5592	$21.60 \pm 0.04$	4	$0.05 \pm 0.03$	$0.4^{+0.2}_{-0.3}$	17 ± 1	14 ± 1	$0.9_{-0.4}^{+0.08} \\ 0.9_{0.3}^{+0.1}$	0.205
	$21.58 \pm 0.07$	$5 \pm 2$	$0.05 \pm 0.05$	$0.4 \pm 0.4$	$17 \pm 2$	$14 \pm 2$	$0.9^{+0.1}_{0.3}$	0.200
12-5869	$20.79 \pm 0.09$	4	$0.25 \pm 0.06$	$2.1 \pm 0.5$	$19.8 \pm 0.5$	$16.6 \pm 0.5$	$0.82 \pm 0.07$	0.495
	$20.78 \pm 0.06$	$4.1 \pm 0.9$	$0.25 \pm 0.04$	$2.1 \pm 0.3$	$19.8 \pm 0.3$	$16.7 \pm 0.3$	$0.82 \pm 0.07$	0.495
12-6072	$22.30 \pm 0.08$	4	$0.04 \pm 0.04$	$0.3\pm0.3$	$17 \pm 3$	$14 \pm 3$	$0.97^{+0.03}_{-0.3}$	0.174
	$22.31 \pm 0.07$	$1.7 \pm 1.2$	$0.09 \pm 0.04$	$0.8 \pm 0.3$	$19.1 \pm 0.9$	$15.9 \pm 0.9$	$0.97 \begin{array}{c} -0.03 \\ -0.3 \\ 0.96 \begin{array}{c} +0.04 \\ -0.2 \end{array}$	0.172
12-8025	$21.05 \pm 0.05$	4	$0.25 \pm 0.05$	$2.1 \pm 0.4$	$20.1 \pm 0.4$	$17.2 \pm 0.4$	$0.79 \pm 0.06$	0.258
	$21.13 \pm 0.03$	$2.4 \pm 0.6$	$0.24 \pm 0.03$	$2.0 \pm 0.2$	$20.0 \pm 0.3$	$17.1 \pm 0.3$	$0.89 \pm 0.06$	0.240
12-8895	$20.6 \pm 0.2$	4	$0.3 \pm 0.1$	$2.9 \pm 0.7$	$20.2 \pm 0.6$	$16.8 \pm 0.6$	$0.42 \pm 0.06$	0.418
	$20.44 \pm 0.04$	$5.0 \pm 0.6$	$0.50 \pm 0.05$	$4.2 \pm 0.4$	$20.9 \pm 0.2$	$17.5 \pm 0.2$	$0.52 \pm 0.04$	0.407
15-4367	$21.81 \pm 0.06$	4	$0.19 \pm 0.04$	$1.6 \pm 0.3$	$20.2 \pm 0.4$	$16.7 \pm 0.4$	$0.22 \pm 0.05$	0.248
	$21.91 \pm 0.03$	$1.9 \pm 0.3$	$0.22 \pm 0.03$	$1.9 \pm 0.2$	$20.6 \pm 0.3$	$17.1 \pm 0.3$	$0.32 \pm 0.06$	0.231
15-5005	$21.69 \pm 0.05$	4	$0.17 \pm 0.05$	$1.4 \pm 0.4$	$19.8 \pm 0.6$	$16.1 \pm 0.6$	$0.74 \pm 0.08$	0.247
	$21.73 \pm 0.03$	$2.2 \pm 0.6$	$0.21 \pm 0.03$	$1.8 \pm 0.2$	$20.4 \pm 0.2$	$16.6 \pm 0.2$	$0.86 \pm 0.08$	0.240
15-7543	$20.86 \pm 0.06$	4	$0.40 \pm 0.06$	$3.0 \pm 0.5$	$20.6 \pm 0.4$	$17.0 \pm 0.4$	$0.79 \pm 0.04$	0.275
	$20.71 \pm 0.08$	$5.0 \pm 0.7$	$0.48 \pm 0.08$	$4.0 \pm 0.7$	$21.1 \pm 0.4$	$17.4 \pm 0.4$	$0.78 \pm 0.04$	0.267
22-0189	$20.32 \pm 0.06$	4	$0.42 \pm 0.06$	$3.6 \pm 0.5$	$20.4 \pm 0.3$	$17.3 \pm 0.3$	$0.49 \pm 0.04$	0.454
	$20.40 \pm 0.04$	$3.2 \pm 0.7$	$0.37 \pm 0.03$	$3.1 \pm 0.3$	$20.2 \pm 0.2$	$17.1 \pm 0.2$	$0.50 \pm 0.04$	0.431
22-1983	$21.33 \pm 0.04$	4	$0.09 \pm 0.04$	$0.7 \pm 0.4$	18 ± 1	15 ± 1	$0.2 \pm 0.2$	0.259
	$21.35 \pm 0.02$	$2.9 \pm 0.8$	$0.09 \pm 0.04$	$0.7 \pm 0.4$	18 ± 1	15 ± 1	$0.2 \pm 0.2$	0.242

 ${\it Table \ 4}$  Morphological parameters of the galaxies in the MUNICS sample

ID	F160W [mag]	n	r <sub>e</sub> [arcsec]	$R_e$ [kpc]	$\langle \mu \rangle_e^{160W}$ [mag/arcsec <sup>2</sup> ]	$\langle \mu \rangle_e^{corr}$ [mag/arcsec <sup>2</sup> ]	b/a	$\chi^2$
S2F5_109 <sup>a</sup> S2F5_109 <sup>b</sup> S7F5_254 <sup>a</sup> S7F5_254 <sup>b</sup> S2F1_357 <sup>a</sup> S2F1_357 <sup>b</sup> S2F1_389 <sup>a</sup> S2F1_311 <sup>a</sup> S2F1_511 <sup>b</sup>	$\begin{array}{c} [\text{mag}] \\ 18.57 \pm 0.03 \\ 18.64 \pm 0.03 \\ 20.42 \pm 0.02 \\ 20.56 \pm 0.03 \\ 19.80 \pm 0.03 \\ 20.99 \pm 0.05 \\ 21.21 \pm 0.03 \\ 20.35 \pm 0.05 \\ 20.43 + 0.03 \end{array}$	4 4 4 4 4 4 4 4	[arcsec] $0.66 \pm 0.03$ $0.67 \pm 0.01$ $0.36 \pm 0.01$ $0.34 \pm 0.01$ $0.41 \pm 0.02$ $0.39 \pm 0.01$ $0.23 \pm 0.02$ $0.18 \pm 0.02$ $0.22 \pm 0.02$ $0.23 \pm 0.01$	[kpc] $5.5 \pm 0.2$ $5.57 \pm 0.09$ $3.00 \pm 0.08$ $2.80 \pm 0.11$ $3.4 \pm 0.1$ $3.28 \pm 0.07$ $1.9 \pm 0.2$ $1.54 \pm 0.15$ $1.9 \pm 0.2$ $1.9 \pm 0.07$	$\begin{array}{c} [\text{mag/arcsec}^2] \\ 19.65 \pm 0.08 \\ 19.77 \pm 0.04 \\ 20.20 \pm 0.07 \\ 20.20 \pm 0.09 \\ 19.9 \pm 0.08 \\ 19.84 \pm 0.06 \\ 19.8 \pm 0.2 \\ 19.52 \pm 0.24 \\ 19.1 \pm 0.2 \\ 19.21 + 0.09 \end{array}$	$\begin{array}{l} [\text{mag/arcsec}^2] \\ 17.14 \pm 0.08 \\ 17.25 \pm 0.04^c \\ 17.68 \pm 0.07 \\ 18.86 \pm 0.09^c \\ 17.08 \pm 0.08 \\ 17.07 \pm 0.06^c \\ 16.9 \pm 0.2 \\ 16.58 \pm 0.24^c \\ 16.2 \pm 0.2 \\ 16.33 \pm 0.09^c \end{array}$	$\begin{array}{c} 0.48 \pm 0.02 \\ 0.49 \pm 0.01 \\ 0.90 \pm 0.01 \\ 0.83 \pm 0.02 \\ 0.67 \pm 0.01 \\ 0.66 \pm 0.01 \\ 0.93 \pm 0.07 \\ 0.86 \pm 0.03 \\ 0.59 \pm 0.05 \\ 0.59 \pm 0.05 \\ \end{array}$	0.320 0.532 <sup>d</sup> 0.265 0.402 <sup>d</sup> 0.312 0.440 <sup>d</sup> 0.312 0.340 <sup>d</sup> 0.269 0.343 <sup>d</sup>
S2F1_42 <sup>b</sup> S2F1_142 <sup>b</sup> S7F5_045 <sup>a</sup> S7F5_045 <sup>b</sup> S2F1_633 <sup>b</sup> S2F1_633 <sup>b</sup> S2F1_443 <sup>a</sup> S2F1_443 <sup>a</sup>	$\begin{array}{c} 20.43 \pm 0.03 \\ 20.06 \pm 0.03 \\ 19.95 \pm 0.03 \\ 19.73 \pm 0.02 \\ 19.61 \pm 0.03 \\ 20.98 \pm 0.03 \\ 20.36 \pm 0.03 \\ 20.96 \pm 0.08 \\ 20.30 \pm 0.03 \end{array}$	4 4 4 4 4 4 4	$\begin{array}{c} 0.23 \pm 0.01 \\ 0.62 \pm 0.03 \\ 0.35 \pm 0.01 \\ 1.00 \pm 0.02 \\ 1.13 \pm 0.04 \\ 0.31 \pm 0.02 \\ 0.26 \pm 0.01 \\ 0.81 \pm 0.06 \\ 0.72 \pm 0.03 \end{array}$	$\begin{array}{c} 1.91 \pm 0.07 \\ 5.2 \pm 0.2 \\ 2.95 \pm 0.7 \\ 8.5 \pm 0.2 \\ 9.53 \pm 0.33 \\ 2.6 \pm 0.1 \\ 2.23 \pm 0.07 \\ 6.9 \pm 0.5 \\ 6.13 \pm 0.24 \end{array}$	$\begin{array}{c} 19.21 \pm 0.09 \\ 21.02 \pm 0.09 \\ 19.67 \pm 0.06 \\ 21.73 \pm 0.05 \\ 21.87 \pm 0.09 \\ 20.4 \pm 0.1 \\ 19.46 \pm 0.08 \\ 22.5 \pm 0.2 \\ 21.6 \pm 0.1 \\ \end{array}$	$\begin{array}{c} 16.33 \pm 0.09 \\ 18.05 \pm 0.09 \\ 16.70 \pm 0.06^{\text{C}} \\ 18.72 \pm 0.05 \\ 18.10 \pm 0.09^{\text{C}} \\ 17.4 \pm 0.1 \\ 16.42 \pm 0.08^{\text{C}} \\ 19.0 \pm 0.2 \\ 18.1 \pm 0.1^{\text{C}} \end{array}$	$0.59 \pm 0.01$ $0.79 \pm 0.02$ $0.73 \pm 0.01$ $0.70 \pm 0.02$ $0.69 \pm 0.01$ $0.56 \pm 0.02$ $0.53 \pm 0.01$ $0.81 \pm 0.05$ $0.76 \pm 0.02$	0.343 0.309 0.915 <sup>d</sup> 0.389 0.394 <sup>d</sup> 0.301 1.258 <sup>d</sup> 0.252 0.676 <sup>d</sup>

 $<sup>^{\</sup>mathrm{a}}$  our best fit parameters for MUNICS sample

 $<sup>^{\</sup>mathrm{b}}$  best-fit model from Longhetti et al. (2007)

 $<sup>^{\</sup>mathrm{c}}$  mean effective surface brightness correction includes K correction and  $(1+z)^4$  dimming factor

 $<sup>^{\</sup>rm d}~\chi^2$  of our fit with the parameters from Longhetti et al. (2007)

The correlation between color and morphological type is not as strong for the red galaxies, as a number of studies have shown. At redshifts near unity, red R-K or I-K selected samples contain roughly as many disk as early-type galaxies (e.g., Moustakas et al. 2004; Yan & Thompson 2003, etc.). At higher redshifts red selected samples also show a mix of morphologies, as shown for the  $z\sim 1.5$  range in Paper VIII and at z>2 by Labbé et al. (2005), Stockton et al. (2004), and others.

#### 4.2. Surface Brightness Profiles & Sizes

Azimuthally averaged surface brightness profiles presented in Figure 3 confirm that six of our 10 GDDS galaxies are well-fit by  $R^{1/4}$  profiles. The effective radii for these six objects range from as small as 0.05 to as large as 0.42, or from 0.4to 3.6 kpc. The median effective radius is 0".26 or 2.2 kpc. As Figure 1 shows, for the most part the 2-D models fit the data well and the residuals are not significantly greater than the sky noise. In 12-8895 and 12-5869 there appear to be some non-axisymmetric structures within the central one arcsecond, while in 12-6072 the model is too peaked. Four of our 10 GDDS galaxies are clearly better fit by  $R^{1/n}$  profiles with indicies near 2, rather than the  $R^{1/4}$  law. These are: 12-6072, 12-8025, 15-4367 and 15-5005. As can be seen in Figure 3 the significance with which the  $R^{1/4}$  law fit is rejected in these objects is low except in the case of 12-8025 where the outer isophotes depart strongly from the  $R^{1/4}$  law profile.

The effective radii of the GDDS galaxies are smaller than those of present-day cluster ellipticals and early-type field galaxies. The median effective radius for low redshift cluster ellipticals is  $\sim 4 \text{ kpc}$  (Jørgensen et al. 1995; Schombert 1986), and the field early type galaxies at  $z \sim 0.5$  from the CFRS (Schade et al. 1999) have a fairly similar median size. The hosts of luminous radio galaxies at  $z \sim 0.8 - 1$  studied by Zirm et al. (2003) probably represent the most massive end of the field & group early type populations at these redshifts. Their sizes are also similar to the lower redshift samples and larger than the GDDS elliptical galaxies that have median effective radius of 2.2 kpc. In contrast, the distant red galaxies (DRGs), defined by their J-K colors, at 2 < z < 3 have a median effective radius of 1.4 kpc

(Toft et al. 2007), somewhat smaller than the passive GDDS galaxies in our sample at  $z \sim 1.7$ .

The sizes of the GDDS passive galaxies appear to support a fairly strong evolution in scale length among the early type galaxies in the 1 <z < 3 interval. A mundane potential explanation for this result is that the under-sampling of the NIC3 PSF data has led to unreliable fits. We can rule out this hypothesis on the basis of three tests. Firstly, we have re-fitted the six galaxies with more finely sampled NIC2 data from the Longhetti et al. (2007) sample, and we recover very similar fits (see Table 4). These fits are shown in Figure 4 using dashed lines to join the values of points obtained by Longhetti et al. (2007) to those obtained by us. Secondly, we have undertaken detailed MC simulations (used to set our error bars in Figure 4) based on generating idealized over-sampled images which are randomly displaced by sub-pixel shifts before being binned to NIC3 resolution and re-fitted. Lastly, two of our objects - 12-5592 and 22-1983 - were observed in the F814W band with ACS on HST. The sizes that we measure for these galaxies, albeit at shorter rest-frame wavelengths, are in good agreement with the sizes derived from our NIC3 data. Thus we are confident that our size determinations are robust.

The strong correction between mass and size, as measured by the effective radius, makes comparisons between the average or median properties of different samples imprecise measures of evolution. The lower redshift samples (z < 1 Jørgensen et al. 1995; Schombert 1986; Schade et al. 1999) cover a broad range of the parent luminosity functions while the higher redshift objects (1 < z < 3), including the DRGs, the GDDS and MUNICS samples (Toft et al. 2007, Paper III, Longhetti et al. 2005), sample the high mass end of the galaxy population and thus are biased to large values in their median sizes. This further strengthens the conclusion that there is strong evolution in the characteristic sizes of early type galaxies above  $z \sim 1$ . The evolution in galaxy sizes can be further quantified by examining the size-mass correlation and its evolution, as is discussed in section 4.4.

#### 4.3. The Kormendy Relation to z = 2

In Figure 4 we present the rest-frame r-band Kormendy relation,  $\langle \mu \rangle_e$  vs.  $R_e$ , for the GDDS

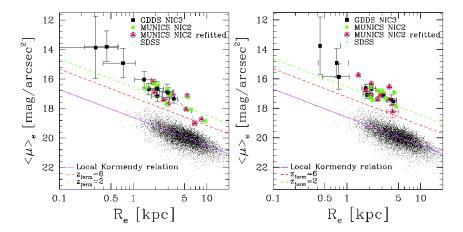


Fig. 4.— Mean rest frame Gunn-r surface brightness within effective radius  $R_e$  as a function of  $R_e$  (Kormendy relation) for objects at redshifts 1.2 < z < 1.9 (GDDS and MUNICS samples) and for the sample of local galaxies (Bernardi et al. 2003, SDSS,). The solid line is the best-fit relation to the SDSS objects. The dashed lines represent the expected luminosity evolution of the local (SDSS, solid line) relation at z = 1.5 for galaxies formed at  $z_{form} = 6, 2$  with exponentially declining SFR and e-folding time  $\tau = 0.1$  Gyr. Different symbols correspond to different samples, and circled triangles denote re-fitted MUNICS sample. Left panel shows  $R^{1/4}$  profile parameters for the galaxies from the GDDS and MUNICS samples, while the right one shows their best-fit  $R^{1/n}$  profile parameters.

and MUNICS samples. As noted earlier, our construction of this diagram is particularly robust because our observed H-band observations match rest-frame r-band at z=1.5 and hence there is negligible residual K-correction uncertainty. We have not applied any evolutionary corrections to the observed surface brightness values. Figure 4 includes the corresponding distribution for present-day early-type galaxies from the SDSS (Bernardi et al. 2003).

Figure 4 shows that the tightness and slope of the Kormendy relation in the GDDS + MUNICS sample is similar to that defined by the local relation. There is a hint that the high-redshift slope may be slightly steeper than the local value, but the difference is not significant. While the highredshift ellipticals fall along a tight Kormendy relation, the relationship itself is offset to higher surface brightness from the low-redshift reference sample. The simplest explanation for this is that is that we are seeing galaxies nearer to their epoch of formation, when they are brighter, and thus the Kormendy relation is shifted upwards. This evolutionary effect cannot fully explain the evolution in the Kormendy relation. The offset in surface brightness compared to the  $z \sim 0$  sample is too

large ( $\sim 2.5$  mag) to be explained by pure luminosity evolution of stellar populations unless the redshift of formation is very recent  $(z_{\text{form}} \lesssim 2)$ , which is inconsistent with both their colors and spectra (see Paper IV) which argue that these are old systems with  $z_{\rm form} \gtrsim 4$ . In the latter case, the maximum dimming allowed is 1 to 1.5 mag, depending on the selected IMF and the star formation history. In addition, we also see from this figure that, in spite of their large masses, typical high-z ellipticals are substantially smaller than their local counterparts. In contrast to the median effective radius for the GDDS sample of 2.2 kpc, early-type galaxies in the SDSS sample presented in Fig. 4 span the range of effective radii with the median value of 4.9 kpc. Finally, we see that three out of ten galaxies in the GDDS sample are 'ultracompact' ( $R_e < 1 \text{ kpc}$ ), and thus are of much higher stellar density. Cimatti et al. (2008) found a similar fraction from ACS imaging and estimate that the number density of comparably dense objects at z = 0 is up to  $10^4$  times lower than at z = 1.5. In contrast, in the MUNICS sample of elliptical galaxies (1.2 < z < 1.7) no 'ultra-compact' objects are found. As we will discuss in the following section, our findings lead us to also conclude that strong size evolution (a factor of 2 or more) is the additional ingredient needed to explain the shift in the Kormendy relation.

## 4.4. The Mass-Size Relation and the Stelar Mass Kormendy Relation

As the previous section illustrates, a proper comparison between galaxy samples at high and low redshifts nearly always entails corrections for luminosity evolution. We can, however, improve on the standard procedure of using simple models of luminosity evolution by using multi-color SED data to fit stellar population models and derive stellar masses for the galaxies in question (this was done and described in Paper III for the GDDS sample). We then recast the data into a new 'stellar mass Kormendy relation' which allows a more fundamental comparison. By doing this we are using the complete set of information (the colors) to measure and remove the luminosity evolution. A further advantage to the use of stellar mass is that it allows us to compare optical and near-IR samples and plot them on the same diagram. A possible disadvantage is that we rely heavily on the mapping from light to stellar mass given by our spectral synthesis modeling, which, in turn, depends on the correctness of our assumptions. So for example derived masses would be in error if the assumed IMF is evolving rather than static.

We consider two projections of the structural evolution that minimize the impact of luminosity and spectral evolution. The first is the size-mass relation, while the second is the relation between stellar mass density and size, which we will refer to as the stellar mass Kormendy relation. In deriving the stellar mass density we assume that the F160W light traces the stellar mass.

In Figure 5 we plot the size-mass relation for our sample. To enhance the usefulness of this figure, we augmented our GDDS and MUNICS data using published measurements obtained for passive galaxies in the redshift range 1.1 < z < 2.0 taken from from two surveys in the HUDF (Daddi et al. 2005b; Maraston et al. 2006), a survey of six galaxies with dominant old stellar population in the fields of radio-loud quasars (McGrath et al. 2007a,b), and GMASS (Cimatti et al. 2008). While McGrath et al. (2007a) use NIC3 F160W observations for their morphological analysis, GMASS (Cimatti et al.

2008) and HUDF (Daddi et al. 2005b) effective radii were measured by fitting ACS F850LP (z band) galaxy images. We corrected all of the stellar mass determinations to a common IMF, using Baldry & Glazebrook (2003) IMF, according to the relations given in Cimatti et al. (2008) and Paper III. Finally, to place our data in a broader context, Figure 5 also shows the size-mass relationship for local early-type galaxies in the SDSS (Bernardi et al. 2003). We recomputed the stellar masses for the Bernardi et al. (2003) SDSS sample using the same prescription applied to the GDDS sample (Baldry et al. 2008; Paper III). The derived masses are in good agreement with those of Kauffmann et al. (2003). The size-mass relationship for early-type galaxies shown in Figure 5 shows a number of interesting features, the most striking of which is that the high-redshift and lowredshift populations show relatively little overlap. In fact, they seem to describe nearly independent loci in size-mass parameter space, with similar slopes, but with galaxies at z = 1 - 2 systematically smaller, at a fixed mass, than galaxies at z = 0. The error bars on individual data points are rather large, but taken as a whole, only  $\sim 25\%$ of high redshift early-type galaxies lie in the region of size-mass space occupied by low-redshift systems.

The size-mass relationship of elliptical galaxies at  $z \sim 0$  is well described by a power law with the same exponent ( $\sim 0.5$ ) as for the earlytypes at  $z \sim 1.5$ . Galaxies with stellar masses of  $8 \times 10^{10} \,\mathrm{M}_{\odot}$ , comparable to M\* today, are approximately three times smaller at  $z \sim 1.5$  than their apparent counterparts today. The number density of compact galaxies with  $R_e < 1$  kpc ('red nuggets') in the redshift range 1.1 < z < 2 is  $2 \times 10^{-5}$  Mpc<sup>-3</sup>. In contrast, number density of these objects in the SDSS sample (Bernardi et al. 2003) is  $3 \times 10^{-8} \text{ Mpc}^{-3}$ , three orders of magnitude lower than that for the higher redshift objects. The 'red nuggets' in two samples are different with respect to mass, too - the median of GDDS compact galaxies mass is  $10^{11} M_{\odot}$ , while the objects of the same compactness in the local Universe have masses with ten times lower median (i.e.,  $10^{10} M_{\odot}$ ). The passive galaxy population at 1.1 < z < 2 span a similar range in stellar mass as galaxies today  $(2 \times 10^{10} - 6 \times 10^{11} \text{ M}_{\odot})$  so, at least at the high mass end, the bulk of the evolution from  $z\sim 2$  to  $z\sim 0$  appears to be in size rather than mass.

In Figure 6 we plot the projected stellar mass density within a radius equal to  $R_e$  (i.e,  $\rho_e=3M_*(R< R_e)/(4\pi R_e^3)$ ) versus  $R_e$  - the stellar mass Kormendy relation. This projection shows the evolution in the structural properties of the passive early-type galaxies very clearly. The z>1.1 galaxies are offset to smaller radii and dramatically higher projected surface mass densities compared to massive early-type galaxies today. Compact objects in the local SDSS sample appear less dense since they are less massive than high redshift objects with the same size. In the density space populated by red nuggets at higher redshifts ( $\rho_e>10^{10}~\rm M_\odot~kpc^{-3}$ ), there are no galaxies in the SDSS sample, implying that number density of these objects at z=0 is  $\lesssim 4\times 10^{-9}~\rm Mpc^{-3}$ .

In both figures 5 and 6 we have color coded the symbols according to redshift into two subsamples: 1.1 < z < 1.46 and 1.46 < z < 2. This splits the sample into two equal time intervals of duration 1.1 Gyr and nearly equal sample sizes. There is a significant diffence in the size distributions in the two sub-samples. In the lower redshift sub-sample 6/18 galaxies, or  $\sim 33\%$  of the sample, fall within the range of the local sample, while in the high redshift sample, only 4/25, or  $\sim 17\%$  of the galaxies fall within the locus of the local systems. Thus it appears that the strongest evolution in size is occurring in the 1 < z < 1.5 interval, although as we will describe in the next section, the heterogenous nature of the data does not allow us to conclude this with much confidence. A number of other studies (e.g., Treu et al. 2005) show that  $z \sim 1$  early type galaxies have normal sizes and mass densities.

#### 5. Discussion

The key result of this paper are that the sizes and projected mass densities of early-type passively evolving galaxies have changed very significantly since  $z\sim 2$ . A number of other studies, noted above, have reached similar conclusions in samples with higher and overlaping redshift intervals. Our analysis has removed much of the uncertainty associated with evolutionary corrections in luminosity and spectral shape by dealing with the mass density rather than surface brightness.

There are a number of potential explanations for the dramatic evolution in the sizes and densites of the passive galaxies. If the compact massive galaxies at  $z \sim 2$  are to evolve into massive elliptical galaxies at  $z \sim 0$  they must grow by a factor of 2-3 in size. The two most plausible paths to this evolution are injection of energy into, or the loss of mass from, the central regions. One possibility is that mergers input energy into the stellar systems and increase their equilbrium sizes. The quiescient spectra of galaxies in the same stellar mass range at 1 < z < 1.5 suggest that any such merger be "dry" and produce little star formation and related activity. Dry mergers have been identified as a likely evolutionary path for the compact massive galaxies at z > 2 discussed recently by van Dokkum et al. (2008). The large stellar masses of the compact passive galaxies at z < 2suggest that equal mass mergers cannot be ubiquitous at later epochs. In Figures 5 and 6 we show vectors that approximate the impact of an equal mass merger, based on the simulations performed by Boylan-Kolchin et al. (2006). Galaxies become both larger and more massive and move primarily along the mass-radius and mass-Kormendy relations rather than normal to them. This problem makes this explanation for size evolution unsatisfactory. While there is good evidence for an increase of roughly a factor of two in the total stellar mass density in red sequence galaxies since  $z \sim 1.3$ , this appears to be in the form of new galaxies appearing on the red sequence rather than mass growth in previously passive systems (e.g., Faber et al. 2007; Bell et al. 2004). One could perhaps appeal to many minor mergers to puff up a galaxy's size, but they would have to all be dry to keep a galaxy on the red sequence and numerous enough to have a significant effect, which seems somewhat contrived.

It has been pointed out to us (N. Murray, private communication) that adiabatic expansion is an interesting alternative to dry merging for increasing the size of galaxies. This process has long been familiar to stellar dynamicists (Hills 1980) and been verified by numerical simulation (e.g., Baumgardt et al. 2007). The process has also been used to model the influence of strong stellar winds in conditioning the Galactic globular cluster distribution (Zhao 2002). In the present context, the potential for adiabatic

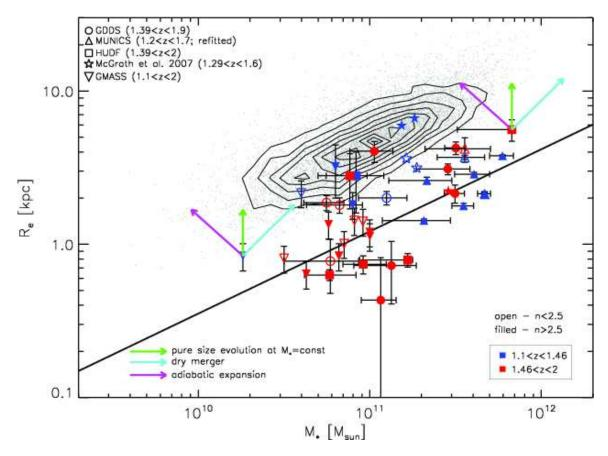


Fig. 5.— Effective radius  $R_e$  as a function of stellar mass for five samples of early-type galaxies in the redshift range 1.1 < z < 2. Points are color-coded by two redshift ranges (red = z > 1.46, blue = z < 1.46). Different symbols correspond to different surveys, with triangles denoting re-fitted object from the MUNICS sample (as in Fig. 4). The size-mass relation for local early-type galaxies in the SDSS is presented with sizes taken from Bernardi et al. (2003), and matched with masses calculated following Baldry et al. (2008) (black points). Contours represent linearly spaced regions of constant density of galaxies in size-mass parameter space. The solid line is the best-fit relation to the data points at redshifts 1.1 < z < 2. Three arrows denote the effects that 1:1 dry merger (Boylan-Kolchin et al. 2006), adiabatic expansion with 50% mass loss, and pure size evolution at constant stellar mass would have on the positions of both the least and the most massive galaxy. See text for details.

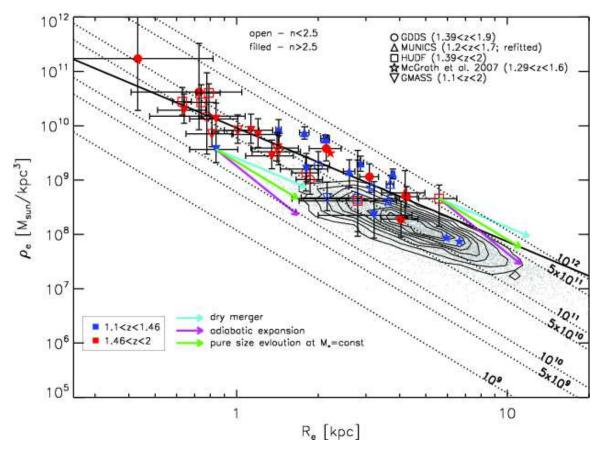


Fig. 6.— Stellar mass density within the effective radius  $R_e$  as a function of  $R_e$  (the "stellar mass Kormendy relation") for five samples of early-type galaxies in the redshift range 1.1 < z < 2. Symbols are as in Fig. 5. The local sample of SDSS galaxies is presented with both points and overlaid contours that denote linearly spaced regions of constant density of galaxies in this parameter space. Dotted lines present the loci of constant total stellar mass, noted on each line in units of  $M_{\odot}$ . The solid line is the best-fit relation to the data points at redshifts 1.1 < z < 2. Three arrows denote the effects that 1:1 dry merger (Boylan-Kolchin et al. 2006), adiabatic expansion with 50% mass loss, and pure size evolution at constant stellar mass. See text for details.

expansion to explain the existence of massive small ellipticals at high redshift is developed in a paper by Murray, Quataert & Thompson (2008, in preparation, hereafter MQT). To motivate the present discussion, a basic version of the some of the key theoretical ideas in the latter paper, kindly communicated to us in advance of publication by the authors, will be applied to the GDDS sample here.

Adiabatic expansion will occur in any relaxed system that is losing mass. As mass is lost the potential becomes shallower, so the system expands in order to relax into a new stable equilibrium. The amount that a system expands depends on both the extent and speed of the mass loss (see Zhao 2002, for details). In general, if a fraction  $\frac{\Delta m}{m} = (m_{\text{initial}} - m_{\text{final}})/m_{\text{initial}}$  of the total mass is lost on a dynamical timescale (or longer), the size of the system increases by a factor of approximately  $\frac{1}{1-\frac{\Delta m}{m}}$ . If the mass is lost more quickly than the dynamical timescale, then the expansion of the system will be larger than this estimate. It is trivial to show that as the system loses mass the dynamical timescale increases in proportion to  $\frac{1}{(1-\frac{\Delta m}{m})^2}$  while the escape velocity decreases as  $1 - \frac{\Delta m}{m}$ , so there are at least two sources of positive feedback leading to further increase the size as the system evolves. Of course, in the extreme case where a significant fraction of the total mass is lost on a short timescale, the system may become unbound.

What processes might lead to mass loss in elliptical galaxies? The obvious candidate is stellar winds from sites of active star formation. However, the early-type galaxies being studied here are relatively red and spectroscopically passive, so winds from young stellar populations are unlikely candidates for mass loss. An interesting alternative is mass loss from evolved A and F-type stars, and we have explored this ideas using the following toy model. We model a galaxy as an instantaneous burst with a solar-metallicity stellar population whose main sequence lifetime (as a function of mass) is that given in Table 5.2 of Binney & Merrifield (1998). We assume that after leaving the main sequence all stars more massive than 8 solar masses wind up as stellar remnants of 1.5 solar mass, and that all stars less than 8 solar masses wind up as remnants with 0.6 solar mass.

We also assume that mass loss from stars is never recycled into future star formation and it outlows far out into the galaxy's potential well, or is lost completely.

In this case,  $\frac{\Delta m}{m}$  as a function of time takes on the form shown in Figure 7 for three initial mass functions (Salpeter IMF, Scalo IMF, and the Baldry & Glazebrook (2003) IMF). Our toy model suggests that  $\frac{\Delta m}{m}$  rises sharply with time until ages of around 2 Gyr, at which point  $\frac{\Delta m(t)}{m(t)}$  flattens out, peaking at around 30% for the Salpeter IMF, and at 50% for the top-heavy Baldry & Glazebrook (2003) IMF. Thus the degree of mass loss from a very top-heavy IMF could explain the size growth. This is shown by the arrows in Figures 5 and 6, which show the effects that 1:1 dry merger (Boylan-Kolchin et al. 2006, cyan arrow), adiabatic expansion with 50% mass loss (magenta arrow), and pure size evolution at constant stellar mass (green arrow) have on the positions of both the least and the most massive galaxies in our sample. However, the timescale over which this occurs poses a huge challenge for explaining the size growth entirely by adiabatic expansion. In this paper we study the size distribution of the population at a time when their the stellar populations are already rather old (see Tables 1 and 2 and discussion in Paper IV) so over the redshift range being probed the galaxies are old enough that the mass loss curves in Figure 7 are already nearly flat. Another constraint on the importance of adiabatic expansion is that is does not explain the steady factor of (at least) three growth in the stellar mass density locked up in massive galaxies over the redshift range 1 < z < 2reported in Paper IV and in other surveys, (e.g., Dickinson et al. 2003; Rudnick et al. 2006), especially on the red sequence (Paper VIII). As the typical mass does not appear to evolve (Fig. 5) this primarily seems to be an evolution in num-

In spite of the problems noted above, adiabatic expansion does appear attractive because it moves the high-redshift distribution shown in Figure 5 in the right direction to match the low-redshift distribution shown in the figure. This is not the case with equal-mass dry mergers, which, as shown by the cyan arrows in the figure, and as noted by previous authors (Boylan-Kolchin et al. 2006), drive evolution along the Kormendy relation rather than

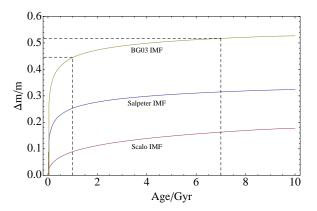


Fig. 7.— The mass loss fraction  $\frac{\Delta m}{m}$  as a function of population age in Gyr, for the simple model described in the text. We assume an instantaneous burst of star formation and show  $\frac{\Delta m}{m}$  as a function of time with three initial mass functions. As expected, the total mass lost is a strong function of the fraction of stars at the high mass end of the IMF. The relative mass loss is small in the age range 1-7 Gyr (dashed lines). See text for details.

displacing the relation itself. While a top-heavy IMF loses enough mass to grow the galaxies by the required factor of two over their complete lifetime, the main problem with the adiabatic expansion model is that to explain our observations that mass loss would have to occur over the age range of 1-7 Gyr, over which Fig. 7 shows only a 5-10 % effect. Ages of the GDDS galaxies are taken from Paper IV, and it is worthwhile to consider whether we might have significantly overestimated the ages of the galaxies in that paper. We think this unlikely for two reasons. Firstly, because broad-band color-based ages for these galaxies seem consistent with ages inferred from spectra of these systems, which often exhibit photospheric features from old stars. Secondly, because changing to a more top-heavy IMF than the Salpeter IMF used in Paper IV would not result in systematically younger ages. In fact the reverse is true, since a more top-heavy IMF would tend to produce synthetic spectra which are bluer for a given star formation history at a given age. So to match the observed colors, any fitting routine would compensate by deriving older ages for the best fit. Quantitatively, we checked the size of this effect by generating models with an exponentially declining star-formation history (e-folding timescale  $\tau = 1$  Gyr) with various stellar metallicities, using both Salpeter and BG03 IMFs (without extinction). We determined that ages using the (top-heavy) BG03 IMF are  $\sim 40-50\%$  larger for

galaxies which are found to be  $\sim 1$  Gyr old using a Salpeter IMF. (Note that derived metallicities using the BG03 IMF are larger too).

Some constraints on the duty cycle for the size change can be inferred from our observations, by noting that the redshift range spanned by our sample is 1.1 < z < 2.0, corresponding to a spread in time of  $\sim 2.2$  Gyr. The division of the sample in half at z = 1.46 using different symbols in Figures 5 and 6 subdivides this redshift interval into two equal time bins, each of which is  $\sim 1.1 \text{ Gyr}$ wide. The sample shown in Figures 5 and 6 contains data from a number of different surveys, and it is certainly unwise to attempt to compare the high-redshift and low-redshift subsets at a detailed level. But it is perhaps worth noting the following very general qualitative trends. Figure 5 appears to show that the character of the size-mass distribution is rather different in the 1.1 < z < 1.46and 1.46 < z < 2.0 intervals, with neither distribution resembling the local data distribution closely. This suggests some degree of evolution between the bins, but with the caveat that these two redshift bins primarily consist of data from different surveys so the strength of the evolution cannot be confidently inferred. On a more speculative note, it can be argued that nothing in Figure 5 rules out the possibility that the high-redshift distribution is evolving into the low-redshift distribution differentially, with different physics operating at the low mass and high mass ends. In fact, some

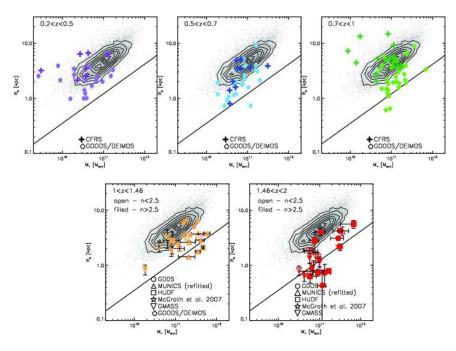


Fig. 8.— As for Figure 5, with data from the GOODS/DEIMOS and CFRS redshift surveys included. Points corresponding to different redshift bins are presented in separate panels. The solid line is the best-fit relation from Figure 5.

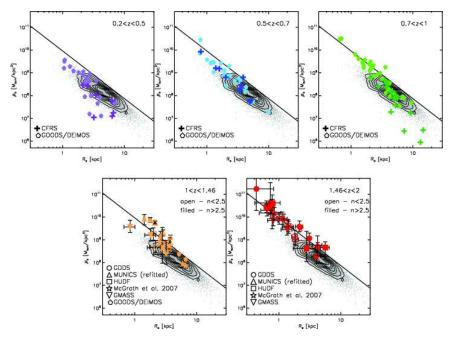


Fig. 9.— As for Figure 6, with data from the GOODS/DEIMOS and CFRS redshift surveys included. Points corresponding to different redshift bins are presented in separate panels. The solid line is the best-fit relation from Figure 6.

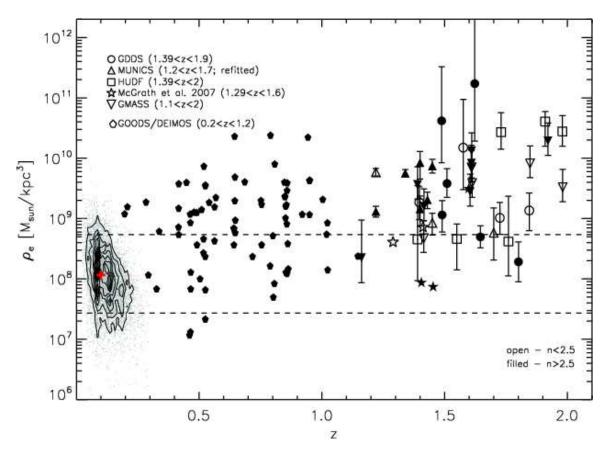


Fig. 10.— Redshift dependence of the stellar mass density within the effective radius  $R_e$ . Symbols are as in Figures 8 and 9. The local sample of SDSS galaxies is presented with both points and overlaid contours that denote linearly spaced regions of constant density of galaxies in this parameter space. Red cross represents the median stellar mass density and the median redshift of the local sample. Limiting stellar mass densities for the 90th percentiles for the SDSS objects with stellar mass densities above and below the median value are given with upper and lower dashed lines, respectively. Following the discussion on the quality of CFRS imaging in section 5 corresponding points are excluded from this fugure.

evidence for this is also hinted at in the figure, which appears to show that the smallest and least massive galaxies lie at z>1.5. It is possible that dry mergers may well be growing the smallest and least massive galaxies along the fundamental plane early in a galaxy's life cycle, before some other process takes over and grows them further in some other way.

It is interesting to contrast the data presented in Figures 5 and 6 with data which spans the redshift range in between the SDSS data and our high-redshift observations. Figures 8 and 9 augment the data in Figures 5 and 6 with intermediate-redshift data taken from the CFRS (Schade et al. 1999; Lilly et al. 1995) and GOODS/DEIMOS (Bundy et al. 2007; Treu et al. 2005) surveys. Effective radii for the CFRS objects are obtained from the WFPC2 814W images. Estimates based on the images in three ACS filters (606W, 814W, and 850W) are available for the GOODS/DEIMOS sample. All objects shown in the upper three panels of figures 8 and 9 have sizes based on the WFPC2 or ACS 814W imaging that translates approximately into the rest-frame V-band for the median redshifts in the 0.2 < z < 0.5 and 0.5 < z < 0.7 panels, and into the rest-frame B-band for the median redshift in the 0.7 < z < 1. panel. GOODS/DEIMOS objects in the 1 < z < 1.46 panel are presented with the effective radii in ACS 850W filter (approximately B-band rest frame). The CFRS masses are obtained following Baldry et al. (2008) and using imaging data of relatively low quality. We note that the difference in the rest-frame wavelengths that are probed at different redshifts makes it impssible to draw any quantitative conclusions about galaxy size evolution. However, figures 8 and 9 show qualitative trends consistent with smooth evolution over the 0.2 < z < 2 range. The dispersion on the size-mass plot in the 0.2 < z < 1regime is large (upper panels in Figures 8 and 9), but there seems to be some evidence for a systematic offest relative to the local trends with the increasing redshift. The GOODS/DEIMOS data in Figures 8 and 9 spans both the low-redshift and high-redshift loci identified in each panel of Figures 8 and 9 by contours and the line of the best fit, respectively. However, the majority of the low-redshift (0.2 < z < 0.5) GOODS/DEIMOS data lie closer to the local relation, in contrast

to the 0.7 < z < 1 panel where the most of the GOODS/DEIMOS points are close to the  $z \sim 1.5$ objects locus. The CFRS data in the 0.7 < z < 1panel of Figure 8 does not seem to follow this trend, and we suggest that it may be due to the shallow imaging of these objects (Lilly et al. 1995). In the lower redshift panels of Figure 8 (z < 0.7) the positions of the CFRS objects are consistent with the GOODS/DEIMOS dataset. In order to compare the number of high mass objects at different redshifts, we use a subsample of 68 GOODS/DEIMOS objects with masses above the GDDS detection limit (see section 2.1). It is interesting to note that relatively few (14/68,  $\sim 21\%$ ) points from the GOODS/DEIMOS subsample have masses greater than  $1.5 \times 10^{11} \ \mathrm{M}_{\odot}$ (M\* at 1 < z < 2, Fontana et al. 2006). In contrast, the high-redshift data set presented in Figures 5 and 6 includes large fraction of objects with  $M_{\star} > M^{*} - 18/43 \ (\sim 42\%)$ . While this could perhaps be consistent with adiabatic mass loss, the arguments presented in our discussion of Figure 7 are compounded by the data presented in Figures 8 and 9 which indicates that size growth is still occurring in galaxies even older than those in our GDDS sample. We think it is likely that the absence of very high mass objects in the GOODS/DEIMOS data is simply due subtle differences in various groups' methodologies for computing stellar masses from photometric data. To further address the question of structural evolution of galaxies presented in Figures 8 and 9 we plot the redshift dependence of the projected stellar mass density (defined in section 4.4) in Figure 10. Dashed lines encompass the range of mass density which contains 90% of the local (SDSS) data points. The median stellar mass density of the SDSS galaxies is  $\rho_e = 1.1 \times 10^8 \mathrm{M}_{\odot} \mathrm{kpc}^{-3}$ and this value is denoted by a red cross plotted at z = 0.1 in Figure 10. Large fraction (88%) of the GOODS/DEIMOS objects have mass densities above the local median value, and 65% of these galaxies have mass densities above the upper dashed line in the figure. For the 1.1 < z < 2sample the corresponding numbers are 90% and 77%, respectively. On this basis we can conclude that the stellar mass density increases over an extended redshift range, though the dispersion of the plot is large, and more points in both intermediate and high redshift regime are needed to properly

constrain this redshift dependence. We intend to revisit the topic in a future paper.

On balance, we conclude that at present neither adiabatic expansion nor equal-mass dry mergers seem able to explain the size growth in early-type galaxies. A successful model will have to simultaneously explain the size change in the galaxies, the duty cycle for this size change, and the epoch in a galaxy's life history at which the change occurs. And, as noted above, mass density growth over the redshift interval being probed suggests that the size growth being witnessed is operating within a broader context for galaxy formation. Over the redshift interval where early-type galaxies are growing in size, the volume-averaged stellar mass density in massive galaxies is increasing, and the morphological mix is changing.

#### 6. Conclusions

The size-mass relationship for early-type galaxies evolves significantly from z=2 to z=1. Over the whole of this redshift range early type galaxies tend to be a factor of 2-3 smaller than local counterparts of similar mass. Similarly compact galaxies are seen at z > 2 (van Dokkum et al. 2008), and we speculate that the very compact galaxies studied in the present paper are simply the evolved counterparts of these higher-redshift objects, caught at a time before subsequent size growth. By comparing the size distribution of our sample with that of lower redshift surveys, we conclude that significant size growth is probably occurring over the redshift range explored in the present paper. The physics of this growth remains mysterious. By comparing the size-mass relation at  $z \sim 1.5$  with its local counterpart we conclude that equal mass dry mergers play only a limited role in growing early-type galaxies, at least once they are older than a few Gyr. Other processes may be as important as dry merging in growing early-type galaxies. Adiabatic expansion is one such process that we have examined, and while it may be important in growing young early-type galaxies, it is hard to see how this mechanism can be invoked to obtain a factor of two growth in the sizes of galaxies as old as those in the present survey.

#### Acknowledgments

We thank Norm Murray for generously sharing his ideas and papers in advance of publication. We also thank Kevin Bundy for useful discussions.

This paper is based on observations obtained at the Gemini Observatory, which is operated by the Association of Universities for Research in Astronomy, Inc., under a cooperative agreement with the NSF on behalf of the Gemini partnership: the National Science Foundation (United States), the Particle Physics and Astronomy Research Council (United Kingdom), the National Research Council (Canada), CONICYT (Chile), the Australian Research Council (Australia), CNPq (Brazil) and CONICET (Argentina).

Based on observations made with the NASA/ESA Hubble Space Telescope, obtained at the Space Telescope Science Institute, which is operated by the Association of Universities for Research in Astronomy, Inc., under NASA contract NAS 5-26555. These observations are associated with program #9760. Support for program #9760 was provided by NASA through a grant from the Space Telescope Science Institute, which is operated by the Association of Universities for Research in Astronomy, Inc., under NASA contract NAS 5-26555.

RGA thanks NSERC, the Government of Ontario, and the Canada Foundation for Innovation for funding provided by an E. W. R. Steacie Memorial Fellowship.

#### REFERENCES

Abraham, R. G., et al. 2004, AJ, 127, 2455 (Paper I)

Abraham, R. G., et al. 2007, ApJ, 669, 184 (Paper VIII)

Baldry, I. K., & Glazebrook, K. 2003, ApJ, 593, 258

Baldry, I. K., Glazebrook, K., & Driver, S. P. 2008, MNRAS(in press), arXiv:0804.2892

Baumgardt, H., & Kroupa, P. 2007, MNRAS, 380, 1589

Bell, E. F., et al. 2004, ApJ, 608, 752

Bell, E. F., et al. 2006a, ApJ, 652, 270

Bell, E. F., et al. 2006b, ApJ, 640, 241

- Bernardi, M., et al. 2003, AJ, 125, 1817
- Binney, J., & Merrifield, M. 1998, Galactic astronomy / James Binney and Michael Merrifield. Princeton, NJ: Princeton University Press, 1998. (Princeton series in astrophysics) QB857.B522 1998
- Boylan-Kolchin, M., Ma, C., & Quataert, E. 2005, MNRAS, 362,184
- Boylan-Kolchin, M., Ma, C., & Quataert, E. 2006, MNRAS, 369,1081
- Brown, M. J. L., Dey, A., Jannuzi, B. T., Brand, K., Benson, A., Brodwin, M. Croton D. J., Eisenhardt, P. R. 2007, ApJ, 654, 858
- Brown, M. J. L., Dey, A., Jannuzi, B. T., Lauer, T. R., Tiede, G., Mikles, V. J. 2003, ApJ, 597, 225
- Bruzual, G., & Charlot, S. 2003, MNRAS, 334, 1000
- Bundy, K., Treu, T., & Ellis, R. S. 2007, ApJ, 665, L5
- Charlot, S., Worthey, G., & Bressan, A. 1996, ApJ, 457, 625
- Chen, H.-W., Marzke, R., McCarthy, P., Martini, P., Carlberg, R. et al. 2003, ApJ, 586, 745
- Cimatti, A., et al. 2002, A&A, 381, L68
- Cimatti, A., et al. 2004, Nature, 430, 184
- Cimatti, A., et al. 2008, A&A, 482, 21
- Daddi, E., et al. 2004, ApJ, 600, 127
- Daddi, E., et al. 2005, ApJ, 631, L13
- Daddi, E., et al. 2005, ApJ, 626, 680
- De Lucia, G., & Blaizot, J. 2007, MNRAS, 375, 2
- Dickinson, M. et al. 2003, ApJ, 587, 25
- Drory, N., et al. 2001, MNRAS, 325, 550
- Eggen, O. J., Lynden-Bell, D., & Sandage, A. R. 1962, ApJ, 136, 748
- Faber S. M., Jackson R. E., 1976, ApJ, 204, 668
- Faber, S. M., et al. 2007, ApJ, 665, 265

- Fontana, A., et al. 2004, A&A, 424, 23
- Fontana, A., et al. 2006, A&A, 459, 745
- Fruchter, A. S., & Hook, R. N. 2002, PASP, 114, 144
- Garmany, C.D. & Conti, P.S. 1985, ApJ, 293, 407
- Gallagher, J. S., Hunter, D. A., & Tutukov, A. V. 1984, ApJ, 284, 544
- Glazebrook, K., et al. 2004, Nature, 430, 181 (Paper III)
- González-García, A. C., & van Albada, T. S. 2003, MNRAS, 342, 36
- Hills, J. G. 1980, ApJ, 225, 986.
- Jedrzejewski, R. I., 1987, MNRAS, 226, 747
- Jørgensen, I., Franx, M., & Kjærgaard, P. 1995, MNRAS, 273, 1097
- Kang X., Jing Y. P., Silk J., 2006, ApJ, 648, 820
- Kauffmann, G., et al. 2003, MNRAS, 341, 33
- Kormendy J., 1977, ApJ, 218, 333
- Kriek, M., et al. 2006, ApJ, 649, L71
- Kriek, M. et al. 2007, ApJ, 669, 776
- Labbé, I., et al. 2005, ApJ, 624, L81
- Le Borgne, D., Rocca-Volmerange, B., Prugniel, P., Lanon, A., Fioc, M., Soubiran, C. 2004, A&A, 425, 881
- Lilly, S. J., Le Févre, O., Crampton, D., Hammer, F., & Tresse, L. 1995, ApJ, 455, 50
- Longhetti, M., et al. 2005, MNRAS, 361, 897
- Longhetti, M., et al. 2007, MNRAS, 374, 614
- Maraston, C., et al. 2006, ApJ, 652, 85
- McCarthy, P. J., Carlberg, R., Chen, H.-W., Marzke, R., Firth, A., et al. 2001, ApJ, 560, L11
- McCarthy, P. J., et al. 2004, ApJ, 614, L9 (Paper IV)
- McCarthy, P. J., et al. 2007, ApJ, 664, L17

McGrath, E. J., Stockton, A., & Canalizo, G. 2007, ApJ, 669, 241

McGrath, E. J., et al. 2007,  $\operatorname{ApJ}(\operatorname{submitted})$ ,  $\operatorname{arXiv}$ : 0707.1050

Moustakas, L. A., et al. 2004, ApJ, 600, L131

Murray, N., Quataert, E., & Thompson, T. A. 2008 (in preparation)

Naab, T., Johansson, P. H., Ostriker, J. P., & Efstathiou, G. 2007, ApJ, 658, 710

Peng, C. Y., Ho, L. C., Impey, C. D., & Rix, H.-W., 2002, AJ, 124, 266

Pipino, A. & Matteucci, F. 2008, A&A (in press), arXiv:0805.0793

Rudnick, G, et al. 2003, ApJ, 599,847

Rudnick, G. et al. 2006, ApJ, 650, 624

Schade, D., et al. 1999, ApJ, 525, 31

Schombert, J. M. 1986, ApJS, 60, 602

Schweizer, F. 1987, Science, 231, 227

Searle, L., Zinn, R. 1978, ApJ, 223, 82

Stockton, A., Canalizo, G., & Maihara, T. 2004, ApJ, 605, 37

Tody, D., 1993, ASP Conf. Series, 52, 173.

Toomre, A., & Toomre, J. 1972, ApJ, 178, 623

Toft, S., et al. 2007, ApJ, 671, 285

Treu, T., et al. 2005, ApJ, 633, 174

van Dokkum, P. G., et al. 2008, ApJ, 677, L5

van Dokkum, P. G. 2005, AJ, 130, 2647

Yan, L., & Thompson, D. 2003, ApJ, 586, 765

Zhao, H. S. 2002, MNRAS, 336, 159

Zirm, A. W., Dickinson, M., & Dey, A. 2003, ApJ, 585, 90

This 2-column preprint was prepared with the AAS IATEX macros v5.2.